Global Vorticity Shedding for a Vanishing Foil

by

Stephanie Chin Steele

Submitted to the Department of Mechanical Engineering
in partial fulfillment of the requirements for the degree of

Master of Science in Ocean Engineering

at the

MASSACHUSETTS INSTITUTE OF TECHNOLOGY

September 2012

Author .....
Department of Mechanical Engineering
August 10, 2011

Certified by .....
Michael S. Triantafyllou
William I. Koch Professor of Marine Technology, Professor of
Mechanical and Ocean Engineering
Thesis Supervisor

Accepted by .....
David E. Hardt, Professor of Mechanical Engineering
Chairman, Department Committee on Graduate Theses

Global Vorticity Shedding for a Vanishing Foil

by

Stephanie Chin Steele

Submitted to the Department of Mechanical Engineering
on August 10, 2011, in partial fulfillment of the
requirements for the degree of
Master of Science in Ocean Engineering

Abstract

We explore several aspects of the phenomenon we call global vorticity shedding. Global vorticity shedding occurs when an object in viscous fluid suddenly vanishes, shedding the entire boundary layer vorticity into the wake at once. In our experiments we approximate the disappearance of a towed foil by rapidly retracting the foil in the span-wise direction. Global vorticity shedding is in distinct contrast with conventional shedding, in which vorticity is shed from a body from only a few separation points into the fluid. In this work, we show that for a square-tipped vanishing foil at an angle of attack, the globally shed boundary layer vorticity forms into primary vortices, which evolve and eventually amalgamate with secondary vortices to leave two lasting vortices in the wake. The secondary vortices are a result of three-dimensionality in the flow. For a streamlined-end foil, we achieve a simpler and less three-dimensional wake with no secondary vortices, and only one lasting vortex dominating the wake. However, due to the initial vorticity distribution near the streamlined end of the foil, the initial circulation is reduced. We also show that the lasting vortices are capable of producing reasonably large forces on a body through simple potential flow estimations, and that vortex formation times are small, with vortices fully formed nearly instantaneously in the flow. These features are promising for a force transducer using global vorticity shedding to impart large and fast maneuvering forces on an underwater vehicle.

Thesis Supervisor: Michael S. Triantafyllou
Title: William I. Koch Professor of Marine Technology, Professor of Mechanical and Ocean Engineering

Acknowledgments

This work is indebted to Prof. Michael Triantafyllou, Prof. Jason Dahl, and Dr. Gabe Weymouth for inspiration and direction.

The author would also like to thank everyone at the Tow Tank who made working on this project a genuine pleasure: Heather Beem, Audrey Maertens, James Schulmeister, Jeff Dusek, Amy Gao, Haining Zheng, Dilip Thekkoodan, Jacob Izraelevitz, Gabriel Bousqet.

Special thanks to all the Chins, Steeles, and family in Christ for loving prayers.

Contents

List of Figures

Chapter 1

Introduction

In this thesis we will discuss various aspects of a phenomenon we label "global vorticity shedding." Simply put, global vorticity shedding refers to the boundary layer vorticity shedding event that occurs when an object is rapidly vanished from the fluid. This event is in contrast to the traditional shedding event that occurs on a stalled foil, a streamlined body at an angle of attack, or behind a bluff body. In traditional shedding, vorticity enters the fluid through only a few separation points at most on the body, so that a vortex takes some finite amount of time to form and shed from the body. [22] In the case of global vorticity shedding, we show that all of the boundary layer vorticity on the body is shed as soon as the body vanishes from the fluid. Since the boundary layer vorticity in this case is deposited into the fluid almost instantaneously, the vortex formation times are much shorter in this kind of shedding.

In the three-dimensional case, a body vanishing from the fluid can be described as: the body would suddenly dissolve, melt, or simply be removed from the fluid.Since vanishing an object is difficult experimentally, we study this phenomenon under the approximation of rapidly accelerating the object out of the fluid. Specifically, we rapidly accelerate a towed foil in the span-wise direction, and study various two-dimensional image cuts in which the foil *cross section* vanishes from the image plane of view.

In this work, we explore various implications of the global vorticity shedding phenomenon through the context of maneuverability for underwater vehicles.

Chapter two describes the experimental set ups we use. We present an overview of the experiments we perform and the reasons we perform them.

Chapter three describes our square foil studies with a towed square NACA 0012 foil being rapidly retracted in the span-wise direction, with results from PIV analysis and some interpretation with help from three-dimensional simulations.

Chapter four describes analysis on a set of experiments similar to the square-tipped foil case, with the alteration that the foil being retracted is a *streamlined-end* foil, with streamlining geometry smoothing the cross-section chord-wise and thickness-wise near the tip.

Chapter five ties all of these experimental results together in a discussion on the possible advantages we see in exploiting this phenomenon for AUV super-maneuverability.

Finally, chapter six will end our discussion will a summary of results and conclusions, and please be sure to note the acknowledgments page for thanks to all the people with whom this work would not have been possible.

1.1 Motivation for global vorticity shedding

1.1.1 Current state of AUV maneuverability

As mentioned previously, we would like to study global vorticity shedding in the context of, and for the application of, super-maneuverability for underwater vehicles. The design most employed today in the field of underwater robotics is the conventional screw-propeller design. While reliable, proven, and efficient for cruising speeds, screw-propeller vehicle designs are not very maneuverable. For example, the REMUS, a commonly used AUV platform for oceanic data and measurement collection, has a turning radius of 2.9 body lengths (body length: 1.6 meters) while cruising at a speed of 0.5 body lengths per second. [21] There have been numerous innovative variations on the screw-propeller design, for example vehicles with cross-body thrusters that allow for larger turning moments to be exerted on the vehicle body, but these designs try to improve maneuverable by adding 'more of the same' to the conven-

tional design. Is there another way, instead of adding more and more on top of an inherently maneuverability-challenged design, to design a vehicle that can achieve super-maneuverability?

Vehicles such as the Robotuna, developed by Dave Barret at the MIT Towing Tank, the VCUUV (Vorticity Control Unmanned Undersea Vehicle), developed as a successor to the Robotuna by Jamie Anderson at Draper Laboratory, and most recently Finnegan the Roboturtle, developed by Stephen Licht also at the Towing Tank, have started us down this path with biomimetic designs that start with a completely different paradigm than that of the traditional cigar-shaped AUV. Finnegan uses flapping foils for both propulsion and maneuvering, and its turning radius is a much improved 0.77 body lengths (body length: 2.0 meters) traveling at 0.72 body lengths per second. However, animals are still much more agile than man made vehicles. For example, a sea lion that travels at 1 body length per second has a turning radius of merely 0.1 body lengths (body length: 2.4 meters). [21] How do nature's creatures achieve such superior agility? One thing that we see over and over again in biology is maneuvering appendages that change shape in some way in order to transfer vorticity into the surrounding fluid, thus inducing lift and suction forces on the animal's body.

1.1.2 Shape change for vorticity transfer

In biology, some examples of biological maneuvering appendages that change shape to more effectively and efficiently transfer vorticity into the fluid are swift wings, bat wings, bluegill sunfish pectoral fins, and duck feet. Lentink and Muller (2004) have studied swift wings, which are able to rapidly change wing sweep to allow, for example, quick transitions between fast cruising and turning motions. [18] Hubel *et al.* (2009) have studied the kinematics associated with the shape change of bat wings; bat wings are highly deformable and can be varied widely in camber along the wing for maneuvering in flight. [11] Dong *et al.* (2010) have shown that bluegill sunfish use both active and passive deformation in their pectoral fins to transfer vorticity most efficiently to an attached tip vortex, producing high and efficient thrust. [8] Finally, Johansson and Norberg (2003) have shown that duck feet have an interesting

delta wing shape that allows the duck to produce power continuously throughout the power stroke, varying continuously from drag-based to lift-based propulsion. As the feet transition to the lift-based part of the power stroke, a starting vortex is shed into the wake, transferring vorticity into the surrounding fluid. [13]

Similarly, numerous studies on numerical and engineered systems have focused on the transfer of vorticity into the fluid as a result of shape change. Recently, Buchholz and Smits (2006) [4], Buchholz and Smits (2008) [5], von Ellenrieder *et a.l* (2003) [24], and Blondeaux et al. (2005) [3] have investigated the wake structures of finite-span heaving and pitching flapping foils. These studies look at the transfer of vorticity into the fluid as a result of unsteady heaving and pitching of the foil, i.e. changing foil orientation. Childress *et al.* (2006) conducted experiments where a flapper-like body was found to suspend itself against gravity in an oscillatory air flow due to the difference in added mass between the upstroke and down-stroke. The body presented varying frontal area, due to the hinged flaps on the body. [6] Spagnolie and Shelley (2009) completed numerical simulation studies on a two-dimensional cylinder in an oscillatory flow. In the simulation, the frontal area exposed to the flow was controlled actively, and a net force is produced by varying the phase between the shape change and the oscillation of the flow. [20]

1.2 Previous Work

Our studies are not the first studies on vanishing objects in fluids; vanishing objects have been the topic of several studies by some rather important scientists from the early twentieth century, among them, Klein, Taylor, and Prandtl. The first treatise on vanishing objects appeared in Klein's 1910 hypothetical thought experiment on a vanishing coffee spoon. Klein hypothesized how, in an inviscid fluid, a coffee spoon shaped towed object would generate a vortex sheet if the coffee spoon were to disappear. Klein argued that circulation would be generated in the fluid, taking as a physical example how a coffee spoon generates a horseshoe vortex when quickly pulled out of the coffee liquid. The generated vortex sheet can be thought of as the

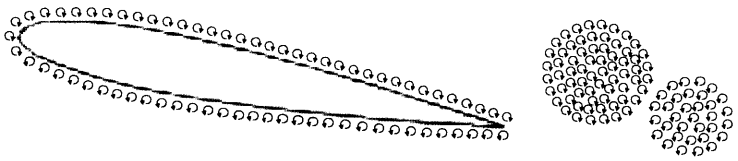

(a) boundary-layer vorticity (b) vortex pair in wake

Figure 1-1: Vorticity in the boundary layer of the vanishing wing redistributes into two wake vortices, conserving the net circulation.

"bound" vortex previously representing the object that is released as a freed vortex once the object disappears. [14]

Taylor (1953) published a theoretical treatise on what would happen in the fluid if a cylinder moving in the bluff body configuration were to suddenly vanish in the fluid. Here, Taylor assumes that the form of the freed vorticity would be a single vortex ring, with a uniform vortex core. These assumptions allow Taylor to calculate the final vortex ring velocity, ring diameter, and vortex core radius, but the theory was never confirmed by experiments, which are difficult to perform. [23]

In 1927, Prandtl conducted a physical experiment in which an accelerated spinning cylinder is rapidly pulled out of the fluid in its span-wise direction. Images of the free surface from the experiment show that a single "freed" vortex is left in the fluid after the cylinder is accelerated out of fluid. The cylinder being accelerated out of the fluid is an approximation to the cylinder vanishing in the flow. Prandtl's experiment is another example of bound vorticity representing the boundary layer vorticity of the object being released as free vorticity into the fluid if the object disappears. [19]

More recently, the MIT Towing Tank group has taken an interest in using this vorticity transfer mechanism for the application of producing large forces for AUV extreme maneuverability. Martin Wibawa (2010) showed in his experiments that a "vanishing" foil, approximated by a towed foil retracted in the span-wise direction, leaves two lasting vortices in the fluid of equal net circulation to that of the bounded vorticity (see Figure 1-1), while an "emerging" foil, meaning a foil entering the fluid in the span-wise direction, causes a starting vortex to be formed. [27]

1.3 Goals of our work

In this thesis, we further the work on the vanishing foil, and we will show results pertaining to the vortex patterns formed, time scales, force production, and the effects of foil geometry for global vorticity shedding.

We aim to answer an assortment of questions related to global vorticity shedding on a vanishing foil in relation to its potential usefulness in the field as a force transducer for extreme maneuverability. The most fundamental question we wish to answer is: what vortex patterns form when the foil vanishes? We have seen from past studies, as discussed above, that bound vorticity is hypothesized to be released into the fluid as freed vorticity, but the form and orientation of the released vorticity cannot be presumed, so we seek to find the form of the freed vorticity after the foil has vanished. We also seek to understand the time scales of this phenomenon, force magnitudes we can expect, and the effect of the streamlined-end foil geometry on the flow features.

Chapter 2

Experimental Set Up

2.1 Overview description of experiment

As mentioned above, the main goal of our studies is to find out what happens to the boundary layer vorticity on a towed foil when the foil "disappears." Since making an object completely vanish is difficult, we approximate a vanishing foil in our experiments by rapidly retracting the foil in the span-wise direction. When we view images from a particular horizontal plane of view, the image of the foil cross section "vanishes" as the foil is retracted out of the plane of view. Thus, our experimental set up consists of a motion control system which tows and retracts the foil through the fluid medium, as well as a high-speed laser and PIV imaging system. The experiments were conducted in a small water tank with dimensions $2.4\,\mathrm{m} \times 0.75\,\mathrm{m} \times 0.75\,\mathrm{m}$. The square foil used in the experiments has a NACA 0012 cross-section, with chord $c = 0.069\,\mathrm{m}$ and span $b = 0.43\,\mathrm{m}$. The foil is mounted, with one end piecing the water surface, to the tank carriage, which moves at a constant forward velocity of $U = 0.2\,\mathrm{m/s}$, so that the experiments are carried out at a Reynolds number of $Re = 14,000$. The motor used for retraction is a Copley Controls STA2504 linear motor, with $\pm 0.35\,\mathrm{mm}$ accuracy. These components are illustrated in Figure 2-1.

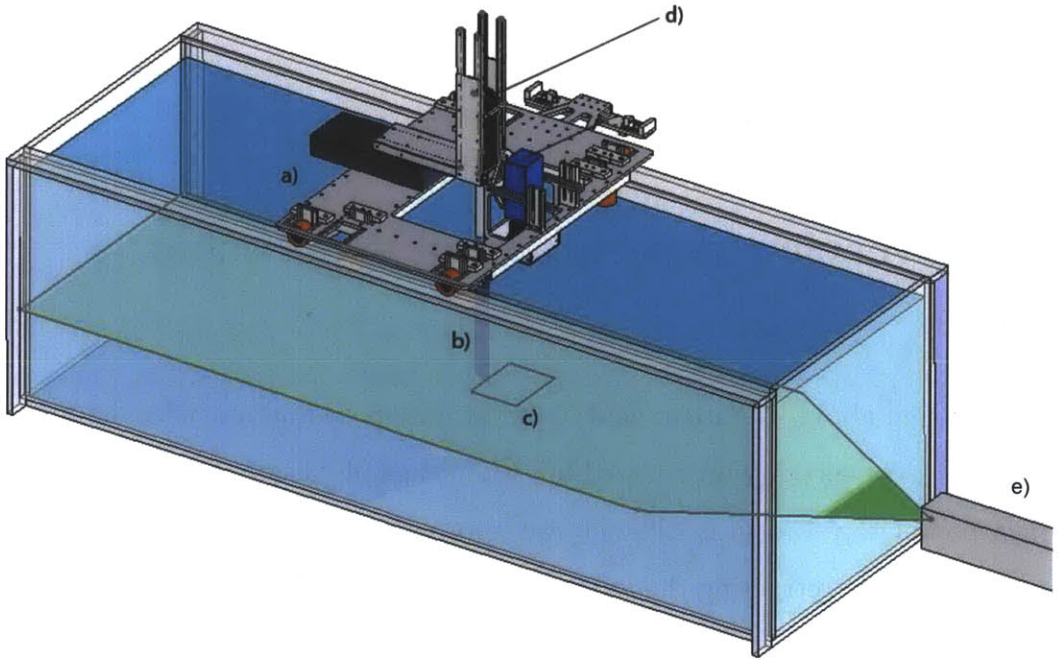

Figure 2-1: Experimental set up assembly with components: a) tank towing carriage, b) NACA 0012 foil, c) horizontal laser imaging plane, d) linear motor, and e) laser head.

2.1.1 Choice of vanishing foil

We chose to study the case of a vanishing foil. If we wished to confirm the theoretical calculations made by Taylor on a vanishing disk, we would use a disk in our experiments in the bluff body configuration, as in the calculations made. However, Taylor's calculations assumed potential flow throughout the motion, and this is physically difficult to realize for a disk in the bluff body configuration; flow separation would yield a drastically different flow from the potential flow prediction. We could also repeat and extend Prandlt's experiments with a vanishing cylinder, but a spinning cylinder does not disturb the flow very much, and thus would not add very much kinetic energy into the fluid. Since our long term goal looks towards vehicle maneuverability, we want to add a lot of kinetic energy to the flow to be able to exploit that kinetic energy, so we can see that a spinning and vanishing cylinder would not get us very far in that goal. Thus, we choose to study a vanishing foil: at small angle of attack separation is minimal, and we are able to disturb and significantly add kinetic energy to the flow.

Also, we choose to conduct experiments at an angle of attack of $\alpha = 10°$ in light of the choices above. We have observed from previous force measurements that for the NACA 0012 foil used in our experiments, this α is the maximum angle of attack before stall occurs.

2.2 Experimental set up: Square foil experiments

2.2.1 Details of motion profile

For the square foil experiments, we use a rectangular-tipped foil, so that the foil cross-section is constant throughout the span. The motor used for retraction is a Copley Controls STA2504 linear motor, with $\pm 0.35\,\text{mm}$ accuracy. As can be seen in Figure 2-2, the foil is towed forward at a constant velocity $U = 0.2\,\text{m/s}$ and when triggered, retracts in the vertical (span-wise) direction at velocity W. The total distance retracted is $\Delta z = 1.44c$, and after that time period vertical retraction is

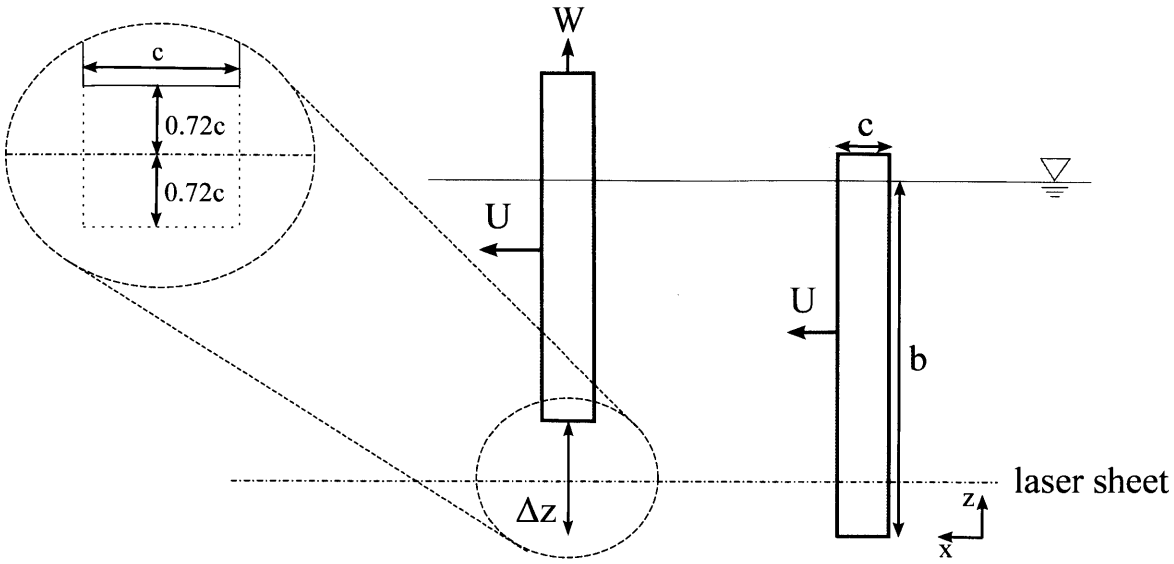

Figure 2-2: Sketch of foil motion during experiment. U is the forward towing speed, W is the vertical retraction speed, and Δz is the total retraction distance. Laser plane is at the midpoint of retraction, at 0.72 times the chord length c.

stopped. At all times the foil travels forward at speed U. For the square foil case, the laser sheet is adjusted to be in the middle of the total retracted distance.

The vertical speed W is controlled by the Copley Conrols STA2504 linear motor and its motion control program, Copley Motion CME2. Thus, the S-curve of vertical position generated through Copley Motion CME2 is plotted in Figure 2-3.

2.2.2 Details of image and data collection

The high-speed camera used to collect images is a 10 bit Imager Pro HS CMOS camera. Images were recorded in single-frame mode with a frame rate of 600 Hz at full resolution (1280 × 1024 pixels). For all experiments, the camera was mounted to the bottom of the tank frame, so that the field of view is looking upward at the bottom of the foil, as sketched in Figure 2-4. The camera was mounted underneath a clear viewing section of the bottom of the tank. For all experiments, foil retraction and image taking was initiated by optical switches so that the foil motion is repeatable. The use of optical switches allows each experimental set of data to be similar in terms of foil position and time within the camera frame, so that sets of data can be averaged to achieve an ensembled flow field.

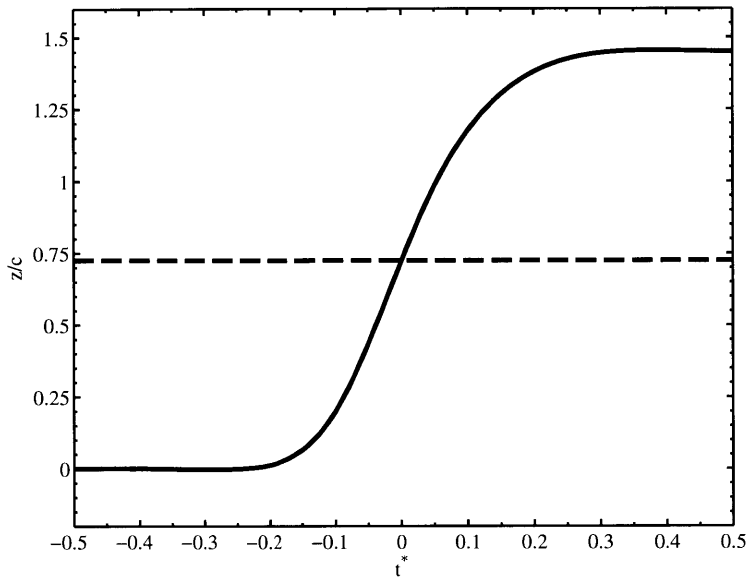

Figure 2-3: Motion profile showing the vertical position of the foil tip plotted against non-dimensional time.

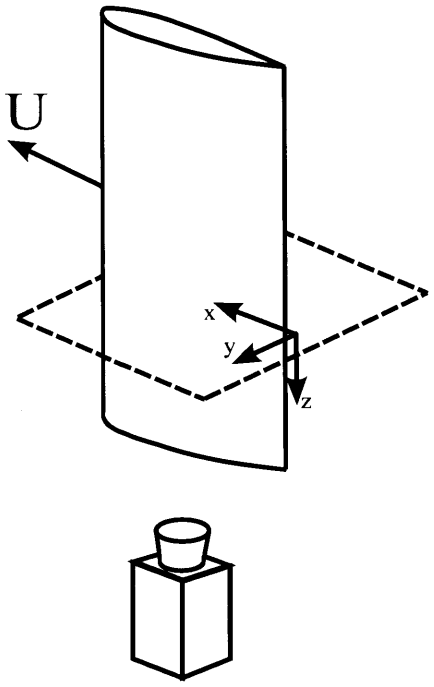

Figure 2-4: Position of high-speed camera with respect to foil and laser plane.

The images were processed for quantitative flow data using a time-resolved PIV system, provided by LaVision GmbH, consisting of a Quantronix Darwin Nd:YLF (λ = 527 nm) single-cavity laser and the above mentioned high speed camera. The pulsed laser beam was collimated and then expanded into a sheet approximately 0.5 mm in thickness to illuminate our horizontal plane of interest, and the fluid was seeded with polyamid seeding particles (PSP), with mean particle diameters of 50 μm.

2.3 Modifications to experimental set up: Geometry studies

For our second set of experiments, we wished to compare the resulting flow structures when the foil used had a streamlined end, meaning that near the tip the cross-section is smoothed in both the chord-wise and thickness-wise directions, and not a rectangular shape, in which the cross-section remains constant throughout the span. The height of the laser plane and geometry of the foils were changes; all other aspects of the experimental set up remain unchanged. Two new foil geometries were used for these experiments. The cross-sections remained a NACA 0012 geometry, and the total chord and span also remained the same. The tip, however, was elliptically smoothed both thickness-wise and chord-wise; one foil was smoothed up to a chord length above the tip , and the other foil was smoothed up to a half chord length above the tip (henceforth referred to as the "full-chord streamlined foil," and "half-chord streamlined foil," respectively). See Figures 2-5 and 2-6 for foil geometry sketches and details.

For the streamlined-end experiments, we performed three additional experiments using our two streamlined-end foils, according to Figure 2-7. All four experiments used the same motion profile, but the laser plane heights and foil used differ in each experiment. The base case experiment with the square-tipped foil had the laser plane at a height of $0.7c$, or 50 mm. The second experiment, labeled *(b)*, uses the full-chord streamlined foil, with the laser plane at a height of $1.1c$, or 75 mm. The third

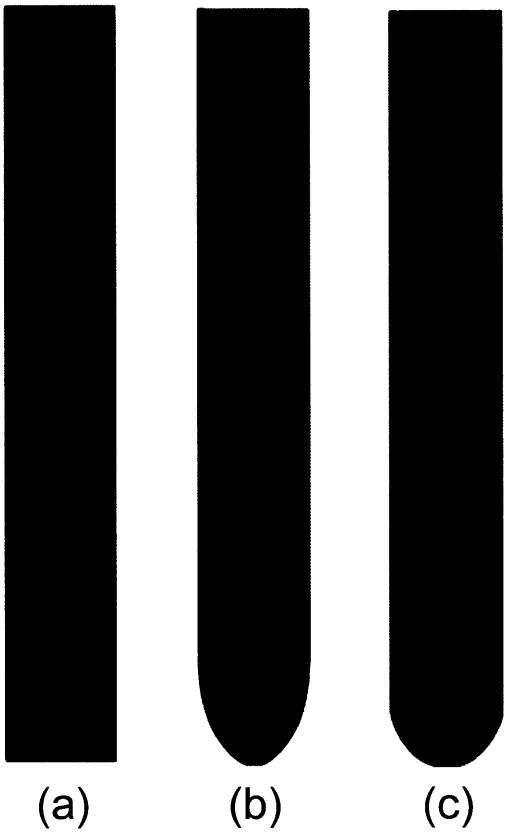

Figure 2-5: Comparison of NACA 0012 foil geometries used in experiments: (a) square-tipped foil, (b) streamlined-end foil with streamlining up to one chord length above tip, and (c) streamlined-end foil with streamlining up to one half chord length above tip.

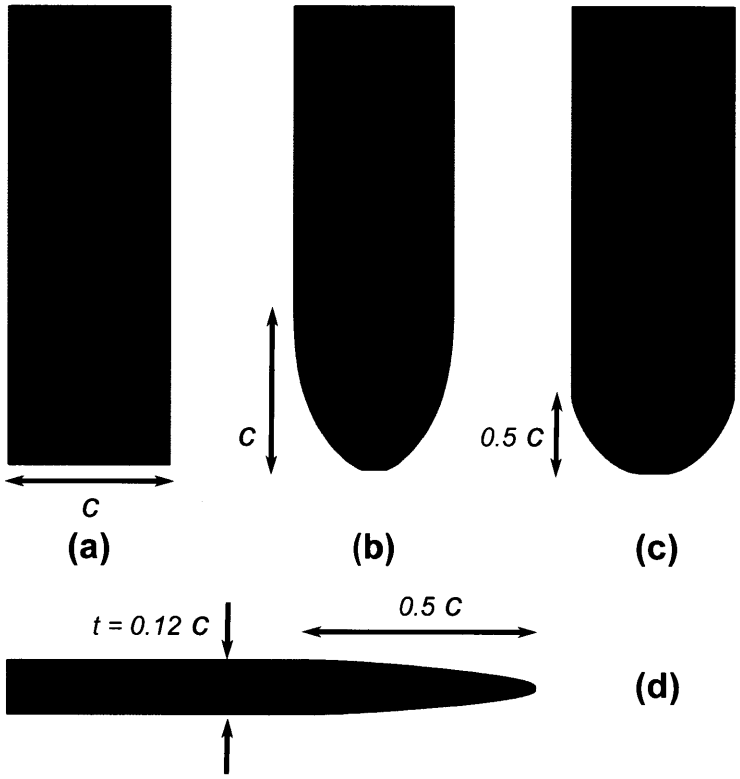

Figure 2-6: Details of foil geometries: (a) square-tipped foil, (b) streamlined-end foil with streamlining up to one chord length above tip, and (c) streamlined-end foil with streamlining up to one half chord length above tip, (d) side view of foil in (c) shows streamlining in thickness direction.

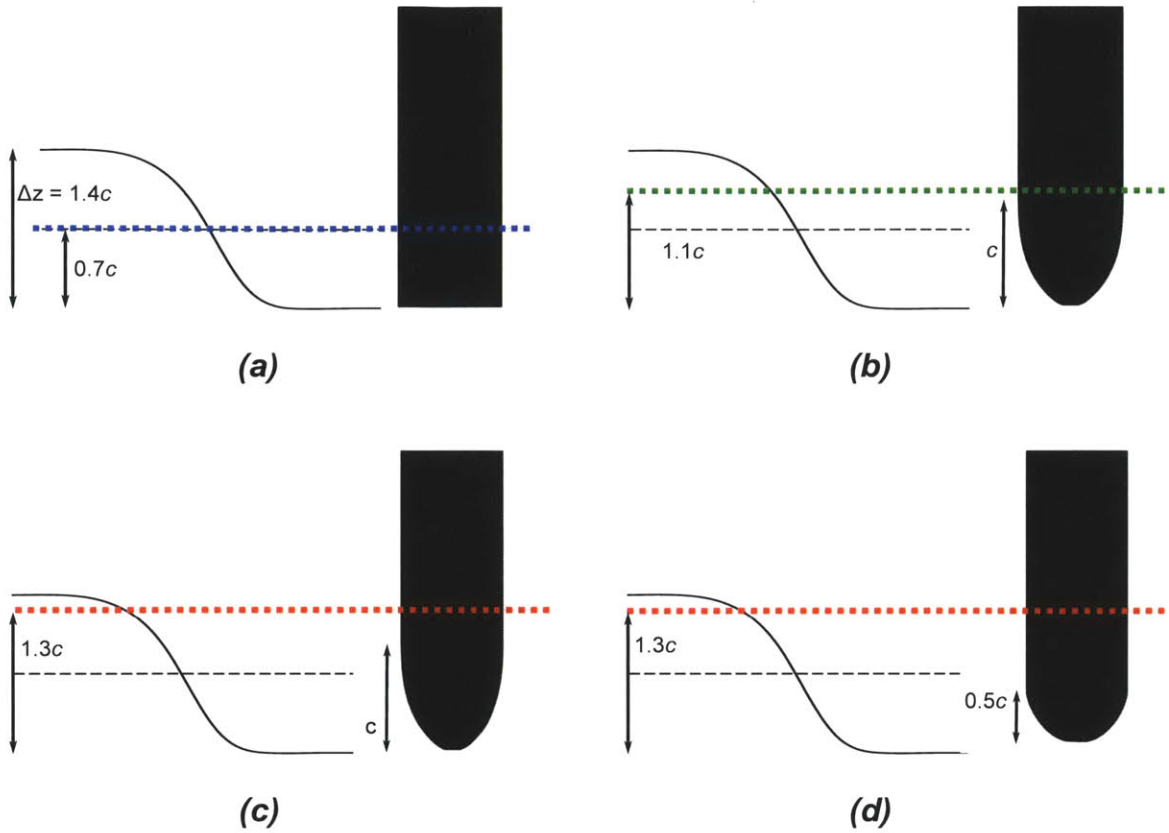

Figure 2-7: The four experiments examined in this thesis use the same motion profile, but have differing laser plane heights and foil geometries. (a) The base case experiment with the square-tipped foil has the laser plane at a height of $0.7c$ (b) Full-chord streamlined foil experiment, with the laser plane at a height of $1.1c$ (c) Full-chord streamlined foil experiment at a laser plane height of $1.3c$ (d) Half-chord streamlined foil experiment at a laser plane height of $1.3c$.

experiment also uses the full-chord streamlined foil, but at a laser plane height of $1.3c$, or 90 mm. Lastly, the fourth experiment uses the half-chord streamlined foil at a laser plane height of $1.3c$. For the square-tipped experiment, we put the laser plane at the mid-motion height, but for the streamlined-end foils we increased the laser plane height in order to reduce tip effects near the streamlined-end portions of the foils.

Chapter 3

Base Case: Square Foil Results

3.1 2D PIV Data

3.1.1 Ensemble-averaged Vorticity Field

As shown in Figure 3-1, we have discerned the vortex patterns associated with the boundary layer vorticity reconfiguration after the foil has vanished, where the vanishing point is defined as $t^* = 0$. Figure 3-1 shows the representative ensemble averaged vorticity field, obtained from averaging each point of the entire vorticity field at each corresponding time step over the 30 performed experimental runs. The vorticity field is shown for different non-dimensional times, over a fine time grid from $t^* = -0.01$ to $t^* = 0.08$ very near the vanishing point, and over a coarser time grid from $t^* = 0.20$ to $t^* = 1.00$.

In the first frame, at $t* = -0.01$, the vorticity field is shown just before the foil has vanished. The foil region and the near foil region is masked in this frame, since we cannot resolve the vorticity field very close to the foil. The dotted line outlines the position of the foil cross-section in the image plane of view. At the instant the foil disappears from the image plane, at $t^* = 0$, we see that the boundary shear layers have deposited into the fluid, and the boundary layer vorticity has nearly instantaneously shed. Here, and in all frames at times afterwards, the dotted outline of the foil shows the horizontal position of the foil even after the foil has left the plane of view.

In the following frames, from $t^* = 0.01$ to $t^* = 0.03$, we see that the free shear layers begin to roll up and form two strong vortices, which we label A and B. While most of the shear layer vorticity rolls up into vortices A and B, not all the shear layer vorticity is entrained into these two vortices. These two vortices remain stable in the flow; no complex motions characteristic of multi-vortex arrangements are observed. [1]

At time $t^* = 0.04$, we see the appearance of what appears to be new vorticity, of positive clockwise rotation, emerging between the two strong vortices previously observed. From $t^* = 0.05$ to $t^* = 0.08$ we can observe the appearance of two secondary vortices, labeled C (negative sign) and D (positive sign). C and D appear to grow in strength and intensity until $t^* = 0.08$, but as time progresses, the strength of the secondary vortices diminishes and ultimately coalesce with the strong vortices A and B. The combination of vortices A and C, and B and D, form the lasting vortices that we observe in the wake at $t^* = 1.00$.

We will see shortly that vortices C and D in the PIV plane result from three-dimensionality of the flow. The sharp edge of the lower end of the foil causes a vortex ring to develop as the foil is retracted. The vortex ring entrains flow and the collapsing boundary layer vorticity with it, so that vortices C and D connect the vortex ring to the vortices A and B, as well as with the tip vortex of the foil.

3.1.2 Circulation Calculations

To investigate further the origins of the secondary vortices C and D that appear in the PIV plane, we calculate the net (non-dimensional) circulation at each time step. The average circulation for times $t^* = 0$ to $t^* = 3.5$ is plotted in Figure 3-2. To calculate the average circulation at a certain time step, the circulation is calculated inside a bounding box for each of the 30 runs at the corresponding time step. The average taken from those 30 circulations is represented by one point on the plot. The bounding box ensures only circulation from the boundary layer is accounted for, excluding the noise vorticity that is present in the wake in the form of Karman street vortices. The bounding box also moves in time, advecting at the same rate as the wake from global vorticity shedding.

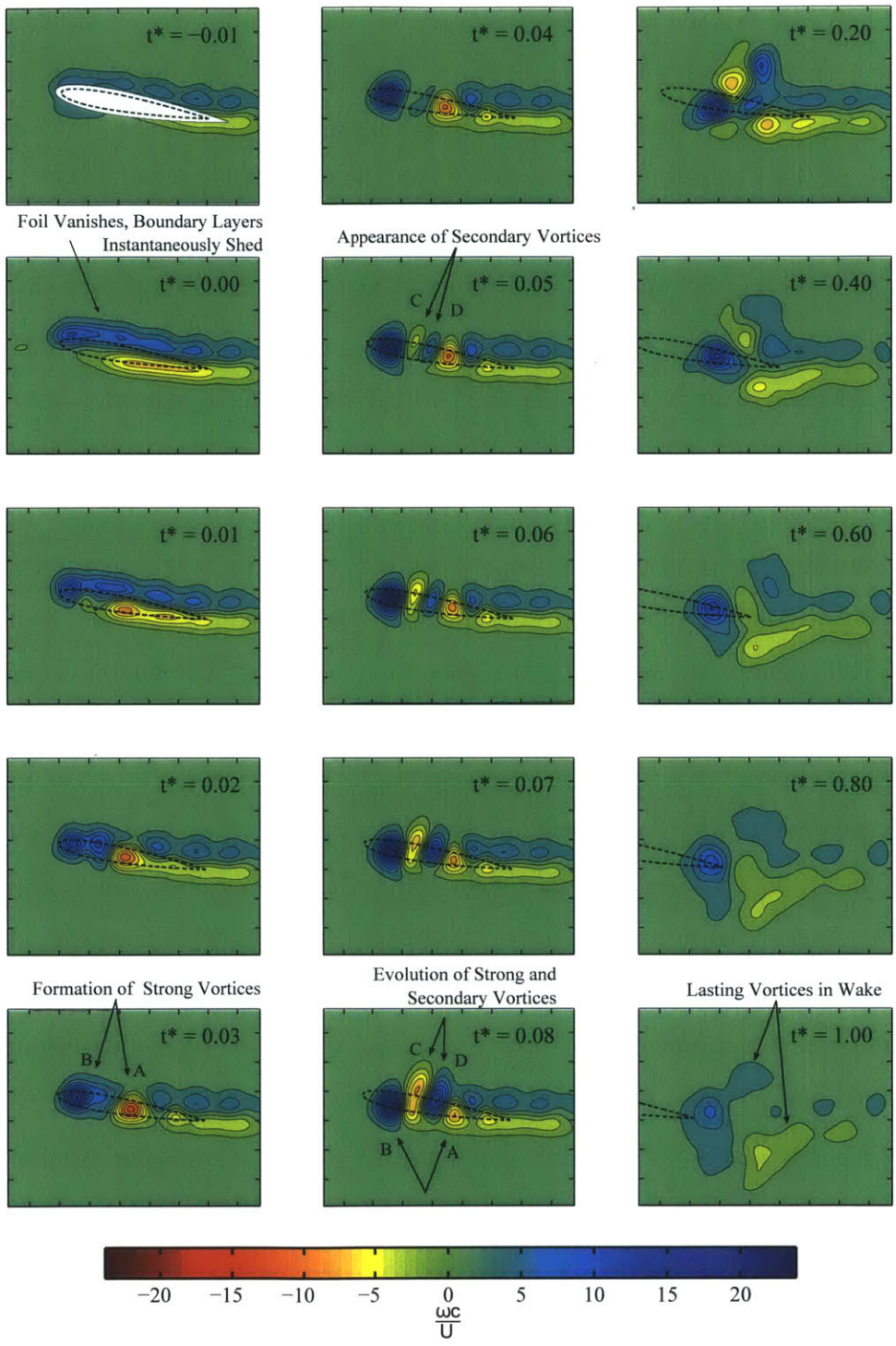

Figure 3-1: Frame by frame sequence of vorticity as measured from laser plane. Foil is traveling right to left in stationary fluid, with foil 'vanishing' from plane at $t^* = 0$, at which point boundary shear layers begin to form vortices A and B. Intermediate vortices C and D are due to three dimensional effects, and later merge with A and B to form the two lasting vortices in the wake. Contours of non-dimensional vorticity show levels of $\frac{\omega_z c}{U} \pm 2.1$. Tick marks on frames show spacing of $0.2c$.

The figure shows the total positive vorticity, the total negative vorticity, and the total net circulation as a function of time. Also depicted are the theoretical values for reference, based on Joukowski's two-dimensional foil theory. The circulation near the initial time of vanishing is close to the theoretical values derived. The theoretical values do not account for finite-span effects or Reynolds number effects, so agreement is good considering the simplifying assumptions used in the Joukowski foil theory.

We see in the figure that the initial positive vorticity and the initial negative vorticity increase from $t^* = 0$ to about $t^* = 0.2$, due to the appearance of vortices C and D, and after the initial growth in the positive curve and the negative curve, the positive vorticity and negative vorticity decay due to mutual annihilation. [17]

Looking at the sum of the positive and negative circulations, which gives us the net circulation, we see that the net circulation remains approximately constant throughout the time span. We see at times closer to $t^* = 0$ that the net circulation does fluctuate slightly, but at later times the net circulation is more smoothly constant. The fluctuations in net circulation is caused by three-dimensionality in the flow, for if the flow is strictly two-dimensional, we know from potential flow theory that the net circulation would remain constant always (since here we assume time scales are too small for viscous effects to take place). After the initial small fluctuations, however, the net circulation in the image plane is equal to the initial value of net circulation right after the foil vanishes, indicating that the effects of three-dimensionality are largely confined to times right after vanishing.

Looking deeper into the cause of the initial growth of positive circulation and negative circulation just after the vanishing time $t^* = 0$, we see that the growth is indeed caused by the "appearance" of vortices C and D in the image plane. Figure 3-3 shows a more detailed calculation of the positive, negative, and net circulations over the time period just after the foil vanishes, from $t^* = 0$ to $t^* = 0.2$. For this more detailed calculation, we define several bounding boxes to not only calculate the circulation of the entire wake area, but to more accurately calculate the circulation contributions of each of the named vortices A, B, C, and D. Within each bounding box isolating a single vortex, then, only positive or negative vorticity is integrated in

the calculation, depending on the sign of the vortex of interest. This is done for each experimental run for each corresponding time step, and averaged to produce the data points on the plot.

Tracking the circulation of each vortex then, we see from the plot that at first, the strong vortices A and B start at an initial value that decreases slowly in time, while the secondary vortices C and D grow in strength. At $t^* = 0$, the value of C and D are close to 0, since they have not appeared in the PIV imaging plane yet. As the secondary vortices enter the imaging plane, their strength increases, while the strength of the strong vortices diminishes. The initial values of the strong vortices are close, but not exactly the same as the initial values shown in Figure 3-2, because as mentioned before, most but not all of the free shear layer vorticity is encompassed into the strong vortices A and B. The strength of vortices C and D finally decay, while vortices A and B regain some strength, and finally, the vortex pairs A and C, and B and D, reach a similar level of strength.

To better understand the meaning of what is happening to all the vortex strength values as time goes on, we can analyze three-dimensional simulations.

3.2 3D Simulations

3.2.1 Vortex structure topology

The key ingredient to understanding where this additional circulation comes from is that due to the sharp lower end of the foil, when the foil retracts we generate additional vorticity in the form of a ring vortex that entrains the flow. To see this, let us examine some results from three-dimensional simulations, done by Dr. Gabriel Weymouth, as seen in Figure 3-4. The Reynolds number, based on the forward speed and the chord length, is set to 14,000, matching the Reynolds number of the experiments. The square foil geometry, angle of attack of 10°, and motion profile also match those of the experiments.

A robust immersed boundary method suitable for dynamic non-deformable bodies

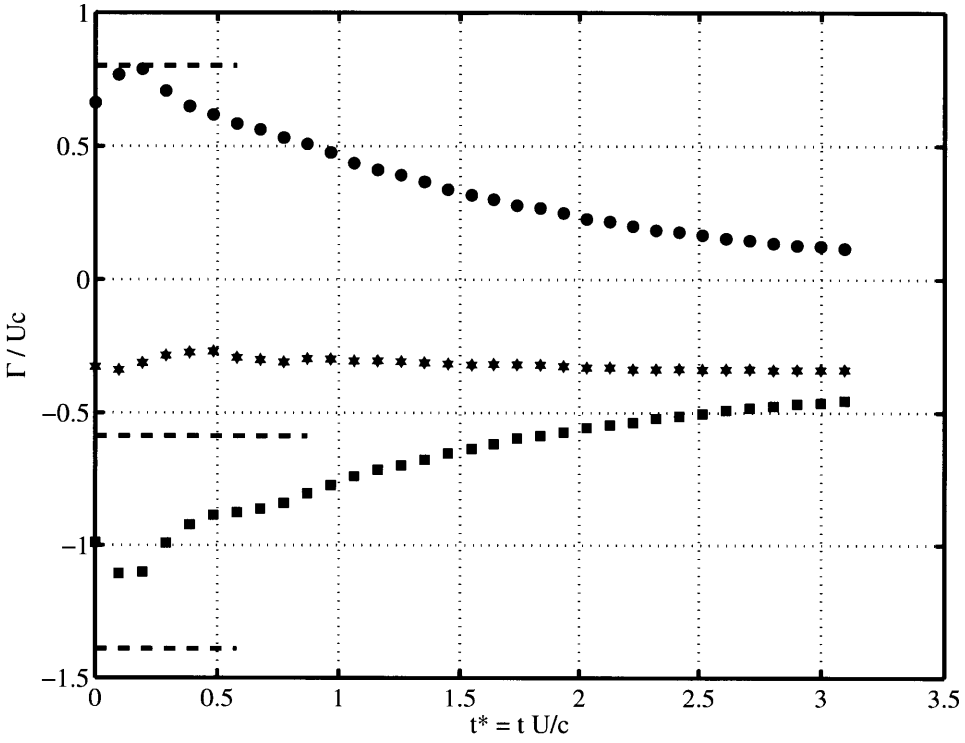

Figure 3-2: Ensembled non-dimensional circulation plotted against t^*. Each point represents an average over the 30 runs at the corresponding time steps. We also plot the circulation derived from potential flow for a Joukowski foil with similar foil geometry for theoretical reference. Total positive circulation, total negative circulation, as well as total net circulation are plotted according to the symbols: ■ – Negative Circulation, ● – Positive Circulation ✱ – Net Circulation, Dashed Line - Joukowski Foil.

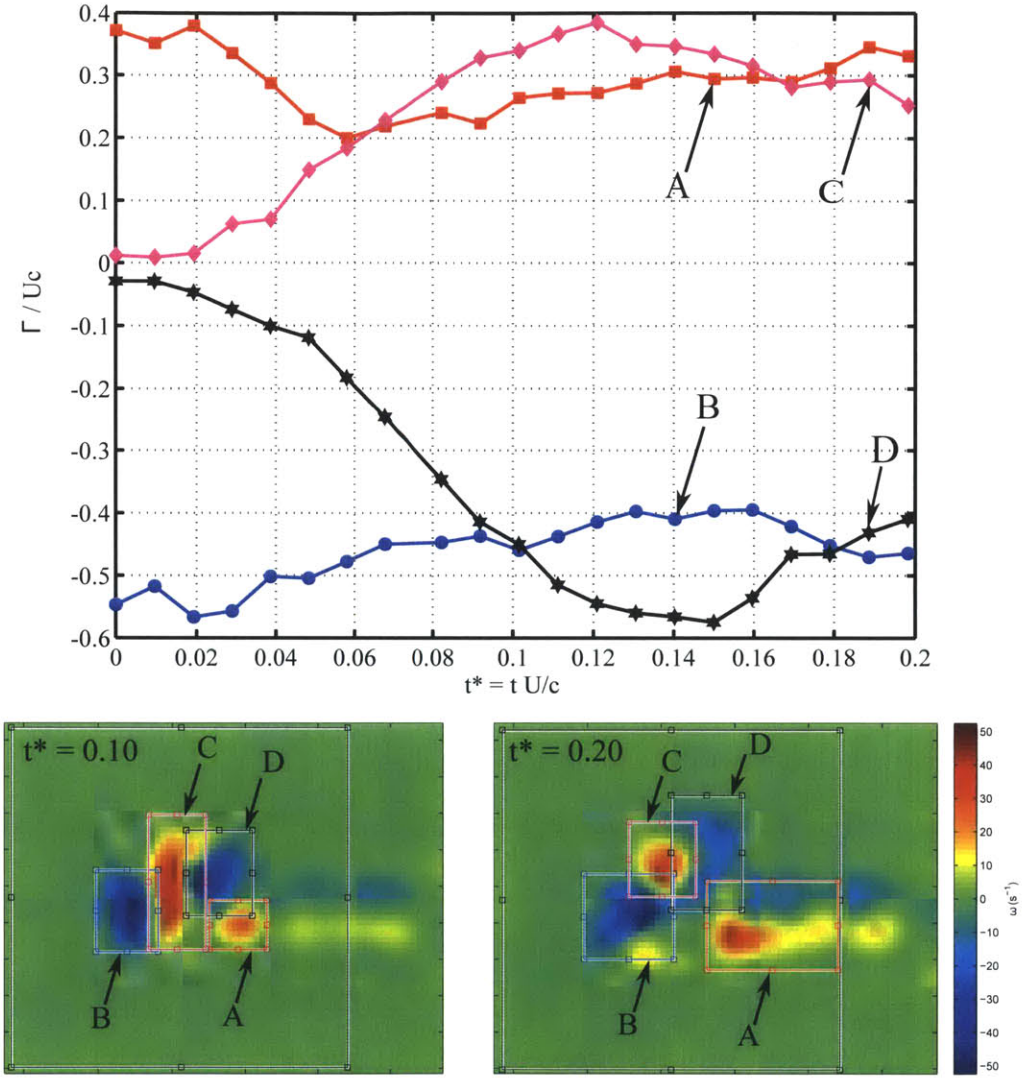

Figure 3-3: A closer look at ensembled non-dimensional circulation of each vortex A, B, C, and D at time steps close to $t^* = 0$. Vortices A, B, C, and D are as referenced in Figure 3-1 and are also labeled for reference on raw data, bottom. Circulation is calculated using bounding boxes to pick out region of interest for each vortex, for each time step for all experimental runs. The average of these values is represented by one data point on the graph.

is used to simulate the flow around the foil. The numerical details of the simulation method follow those used in [25] and [26]. The effect of turbulence is modeled using an implicit large-eddy simulation (ILES) scheme [15], which preserves the time-varying structures in the wake. More than 3.1M grid points are used, with 50 points along the chord length, to ensure resolution of the small-scale features.

Vortex cores in the resulting flow simulation are visualized using iso-surfaces of the λ_2 metric of Jeong & Hussain (1995). [12] The vortex core surfaces are then colored using contours of the z-axis component of the vorticity in order to illustrate the rotation of the vortex cores, where red coloring indicates rotation in the negative z-direction, blue coloring indicates rotation in the positive z-direction, and gray coloring indicates that there is no z-direction component of rotation.

We must note that the vortex cores representing vortex structures A and B (using the same label between corresponding vortices in 2D data and vortex structures in 3D visualizations) do not appear as vortex cores all the way up the side of the foil. Remembering the the bound vorticity is initially shed as a free shear layer, only the vorticity that has already collapsed into vortex structures A and B will appear as vortex cores in these numerical simulation visualizations.

From Figure 3-4, we see three instants in time as the foil is undergoing its vertical retraction.

At $t^* = 0.05$, the tip vortex has bent upward, a ring vortex has formed beneath the foil tip, and the connection between the tip vortex and bound vorticity is beginning to split apart. Vortices A and B are visible at the splitting point, while vortices C and D are not yet fully formed.

At $t^* = 0.13$, the vortex core connections between the tip vortex and the foil are more clearly seen. In this image, the limitation of the vortex core visualization is apparent as vortices A and B must connect to the boundary layer of the foil, which is not visible as a contour of λ_2. As the foil moves upward, the free shear layers left in the fluid collapse to form vortex cores A and B. The formation of a vortex ring R underneath the foil forces the shed free layers to wrap around and entrains part of the shed vorticity upwards, because the ring follows the upward motion of the foil. This

results in the formation of vortices labeled C and D, which connect to the ring and are continuously stretched as the foil is pulled upwards. Also present are additional small core structures present that reconnect the tip vortex to the ring. For instance, vortex C consists of two smaller cores connecting to the tip vortex. This variation in the formation of vortices is also apparent in slight variations between runs of the experimental PIV data.

At $t^* = 0.25$, vortices A and C have coalesced to form one strong vortex tube, and vortices B and D have coalesced to form another strong vortex tube. These two strong vortex tubes are aligned in the span-wise direction of the foil. The alignment and strength of vortices A/C and B/D indicate that at this later t^*, the resulting flow is largely two-dimensional and the three-dimensional effects from the foil tip are not significantly affecting the flow at the midpoint of the span-wise excursion.

3.2.2 Idealized vortex structure topology

The idealization of the time-varying three-dimensional vortex structures present in the flow are sketched in Figure 3-5. We first note that as the foil moves forward at constant speed and constant angle of attack, there is a tip vortex that connects to the lines of circulation on the suction side and pressure side of the foil at the tip. Based on Prandtls lifting-line theory and the tight bundling of vortex filaments in the near wake of a rectangular wing, as found in the near-wake study by Birch & Lee (2005) [2], the tip-vortex circulation has equal strength to that of the bound vortex. Then, when the foil begins to pull up, the tip vortex is tilted at an angle in the flow, as the tip vortex follows the motion of the foil. The tip vortex connects to the shed boundary layer vorticity, which collapses into the two strong vortex structures A and B (labeling of vortices in two-dimensional data match that of vortex structures in three-dimensional visualization). Additionally, when the foil begins to pull up, additional shear layers are generated in the flow due to the sharp lower edges of the rectangular foil, forming a ring-like vortex structure beneath the bottom of the foil, labeled as R. The ring-like structure entrains the flow, including part of the vortex structures A and B that are connected to the tip vortex, labeled as T in the figure.

The part of vortex structures A and B that are entrained by the ring vortex form the secondary vortex structures C and D, which are also still connected to the tip vortex T. Thus, we have new circulation introduced by the ring vortex R, as well as breaks in the connections between the tip vortex T and vortex structures A and B, that connect A and B to the ring vortex R.

Comparing this progression of time varying vortex structures to our previous two-dimensional PIV results, we can now understand why the strong vortices A and B initially decay while the secondary vortices C and D grow in strength. Since the ring vortex initially entrains the flow (and its circulation) near the tip, the ring vortex R breaks the connection between lines of circulation B and T to form a new line of circulation C that connects to R, and breaks the connection between lines of circulation A and T to form a new line of circulation D that connects to R. The ring vortex R entrains away some of the strength of the strong vortex structures A and B, and forms the new vortex structures C and D. There may also be additional circulation fed into A, B, C, and D from ring vortex R, since they are all connected, and this circulation fed from R would explain the sudden increase of circulation in Figure 3-2 that was not there before, since the generated shear layers of R are not present before vertical retraction occurs.

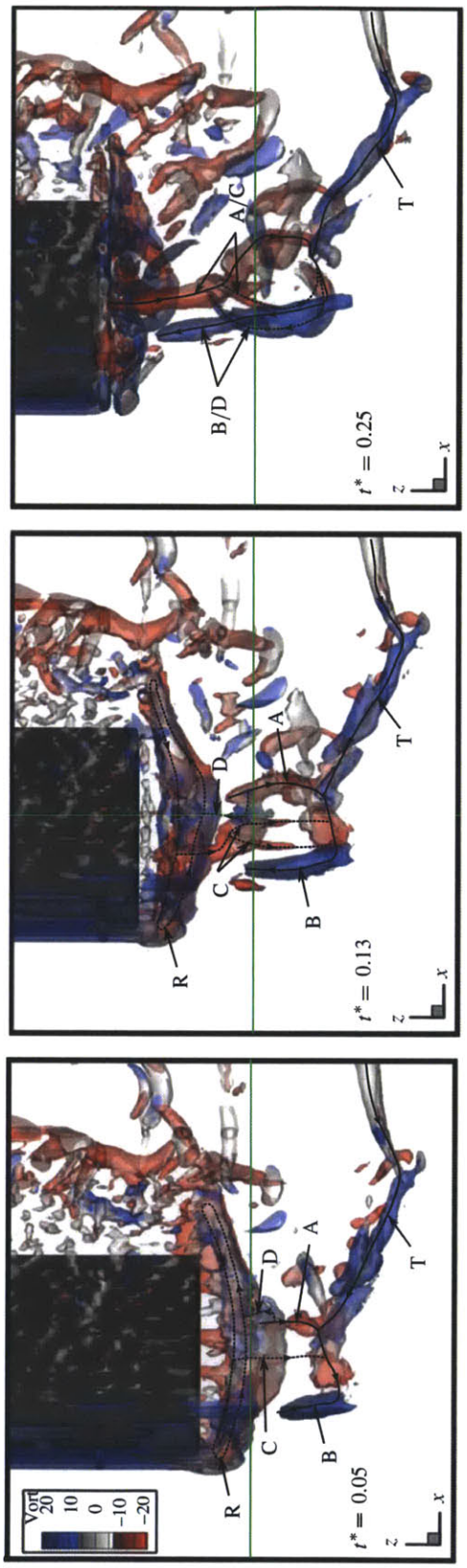

Figure 3-4: Three dimensional simulation of vanishing foil experiments. Colored contours show λ_2 criterion contours of vortex cores present in the flow.

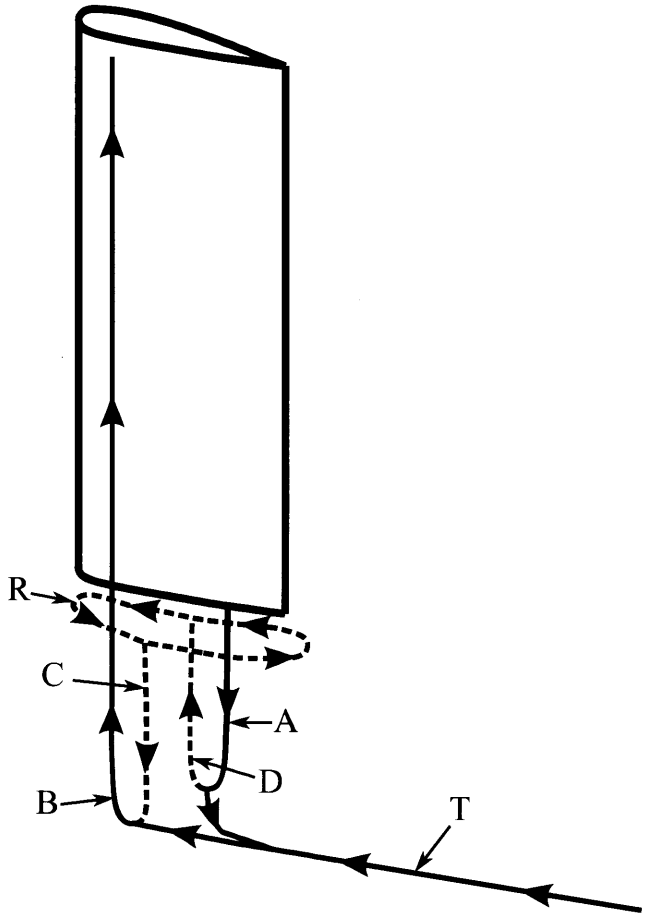

Figure 3-5: Sketch illustrating three dimensional vortex structures present in flow after foil retracts. See text for explanation of vortex structures and their formations.

Chapter 4

Geometry Studies: Streamlined-end Foil Results

4.1 Overview of streamlined-end experiments

Please refer to Chapter 2 for details of the experimental set up for the streamlined-end experiments. In these experiments, we have collected PIV data for the vanishing foil whose end is streamlined up to a full chord length of the span (referred to as the "full-chord streamlined foil"), and for the vanishing foil whose end is streamlined up to a half chord length of the span (referred to as the "half-chord streamlined foil").

We have seen in the previous results section that a vanishing square-tipped foil results in complicated flow features in the local wake due to three-dimensionality in the flow. The formation of the shed ring vortex at the sharp edges of the square foil results in the entrainment of the flow and the appearance of the secondary vortices seen in the PIV experiments. Hence, here, we investigate whether we can create a simpler flow and reduce three-dimensionality by using streamlined-end foils instead of a square-tipped foil.

4.2 2D PIV Data

4.2.1 Ensemble-averaged Vorticity Field

In Figure 4-1, we see a series of images of the ensemble averaged vorticity field from experiment *(d)* of Figure 2-7, with the half-chord streamlined foil. Again, as in the square case, we see an ensemble averaged vorticity field, meaning that we have averaged the vorticity of each point of the entire vorticity field at each corresponding time step over the 15 performed experimental runs, in order to show a representative run emphasizing repetitive flow features and deemphasizing noise. To stay consistent with our earlier definition of the vanishing event when the cross section of the foil leaves the PIV plane (at $t^* = 0$), even though the streamlined-end cross section shrinks smaller and smaller as the foil is pulled upward through the plane, the vanishing event at $t^* = 0$ is defined when the cross section completely disappears from the plane, or when the tip of the streamlined-end foil has left the laser/PIV plane.

In this series of images, we can see that once the foil vanishes, the boundary layer sheds directly into the fluid as two shear layers, as before with the square-tipped case. However, here we see that as time progresses, the shear layers continuously roll up to form the lasting vortices, slowly and continuously, without interruption from any appearance of secondary vortices. The secondary vortices simply do not show up in the streamlined-end experiments, and the progression of the wake formation is indeed less complicated than observed in the square-tipped case.

4.2.2 Circulation Calculations

To understand better the progression of the shear layer roll-up into the lasting vortices in the wake, we calculate the total positive circulation, the total negative circulation, and the net circulation present at each time step. The circulation is calculated within a moving bounding box that captures only the vorticity in the local wake, and excludes vorticity present in the Karman street. For each time step, the circulation is calculated for each of the 15 runs and then averaged, so that one point on Figures

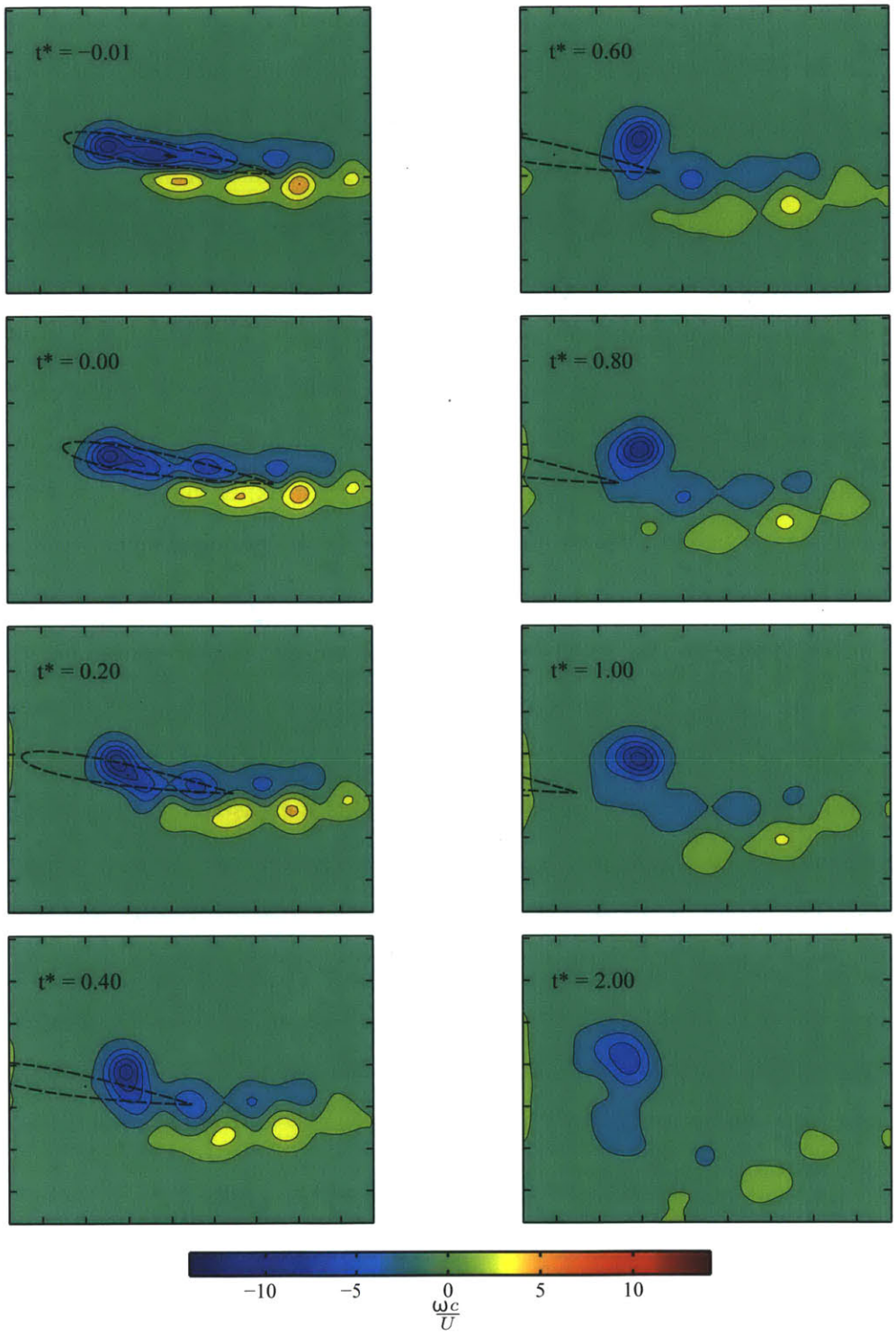

Figure 4-1: Frame by frame sequence of vorticity as measured from laser plane. Half-chord streamlined foil is traveling right to left in stationary fluid, with foil 'vanishing' from plane at $t^* = 0$. Shed boundary layers continuously roll up to form one lasting vortex in the wake. Contours of non-dimensional vorticity show levels of $\frac{\omega_z c}{U} \pm 1.9$. Tick marks on frames show spacing of $0.2c$.

4-2 and 4-3 represents an average over 15 experimental runs. In Figure 4-2, non-dimensionalized circulation is plotted against non-dimensional time for each of the experiments *(a)* through *(d)* as described in Figure 2-7. The results for experiment *(a)*, with the square-tipped foil, are shown again for comparison, in black. The results for experiment *(b)*, with the full-chord streamlined foil at $1.1c$ laser plane height, are shown in blue. The results for experiment *(c)*, with the full-chord streamlined foil at $1.3c$ laser plane height, are shown in green. Lastly, the results for experiment *(d)*, with the half-chord streamlined foil at $1.3c$ laser plane height, are shown in red.

We can see in Figure 4-2 that while the positive, negative, and net circulation values near the larger t^* values are similar for all four experiments, the initial value and initial slopes behave very differently between the square-tipped case and the streamlined-end cases.

Let us first focus on the results of the streamlined-end experiments. For the three streamlined-end cases, the results follow the same trends, which are very close to flat lines for the total positive, total negative, and net circulation lines. The magnitude of the total positive and total negative circulations increase as the foil streamlining becomes confined to a smaller region near the tip, and as the laser plane height increases. This holds as expected, for the shorter the streamlining length and the higher the laser plane, the farther away from tip effects and the closer to theoretical values we expect to measure. Overall, between all the streamlined-end experiments, the results exhibit similar behavior, and so for the remaining analysis we can focus on comparing only the results of the streamlined half-chord streamlined foil against the results of the square foil, for clarity.

Looking at Figure 4-3, we can more closely examine the similarities and differences between the results for our streamlined half-chord streamlined foil case and our square foil case. We have already noted that the streamlined-end foil starts out with smaller magnitude of positive circulation and negative circulation than in the square case, which is not to be unexpected. Since the streamlined-end foil cross section changes shape near the tip, multiple tip vortices are shed along the length near the foil tip and from conservation of circulation, less circulation is expected to act on the foil end.

[9] Another difference between the two sets of results is the slope of the circulation decay. We can see for the square case that after the initial increase in both positive and negative circulation that comes from the injection of the secondary vortices, both lines thereafter decrease until leveling off near the end of the data set. Since we presume our timescales are too small for viscous dissipation to have a chance to act, we hypothesize that the decay of circulation is due to annihilation of vorticity due to three-dimensional mixing. When we look at the streamlined-end data (in red), we see that unlike the square foil case, the total positive and total negative circulation lines remain about constant. There is a slight decrease in the values, but nowhere near the steep decrease seen in the square case. This indicates that in our streamlined-end case, three-dimensionality is indeed reduced. For the values near the end of the data set, at times near $t^* = 3$, the total positive circulation values for both experiments end up at similar values. The total negative circulation, having the stronger magnitude of the two, decays very slightly and as a result, the total negative circulation and the net circulation for the streamlined-end case end up having a larger magnitude than those of the square case near $t^* = 3$. This is also another indication of a less three-dimensional flow; the net circulation value for the streamlined-end case has a larger magnitude and is closer to the theoretical Joukowski foil prediction.

What we conclude here is that in using the streamlined-end foil, we are successful in simplifying the flow structure and reducing the three-dimensionality of the wake, albeit at the expense of lower initial circulation due to the initial vorticity distribution near the tip of the streamlined-end foil.

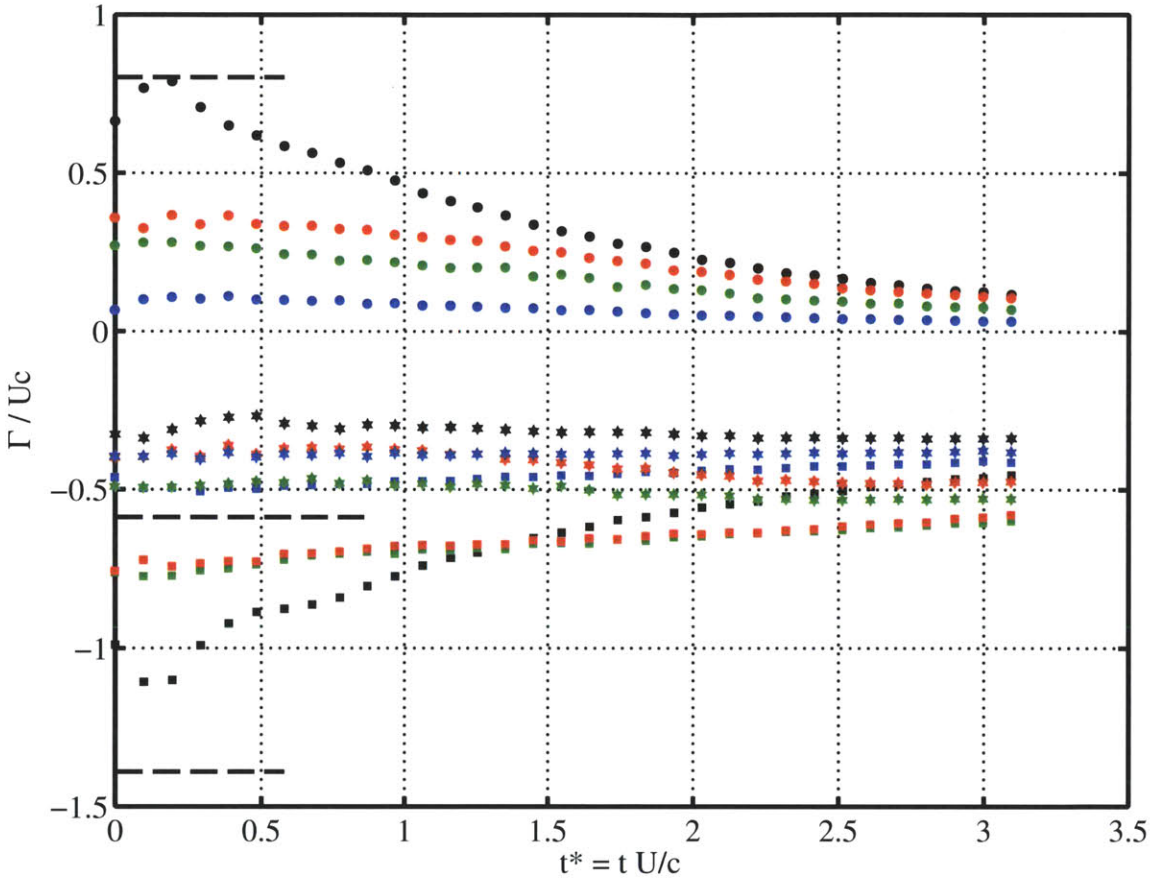

Figure 4-2: Averaged total positive circulation, total negative circulation, and net circulation calculated at each time step. Averaged over 30 experimental runs for the square case, and over 15 runs for each of the streamlined-end cases. Net circulation is simply total positive circulation summed with total negative circulation. Please refer to Figure 2-7: black lines correspond to experiment *(a)*, blue lines to experiment *(b)*, green lines to experiment *(c)*, and red lines to experiment *(d)*. Circulation derived from potential flow for a Joukowski foil with similar foil geometry also plotted for theoretical reference. Total positive circulation, total negative circulation, as well as total net circulation are plotted according to the symbols: ■ – Negative Circulation, ● – Positive Circulation ✱ – Net Circulation, Dashed Line - Joukowski Foil.

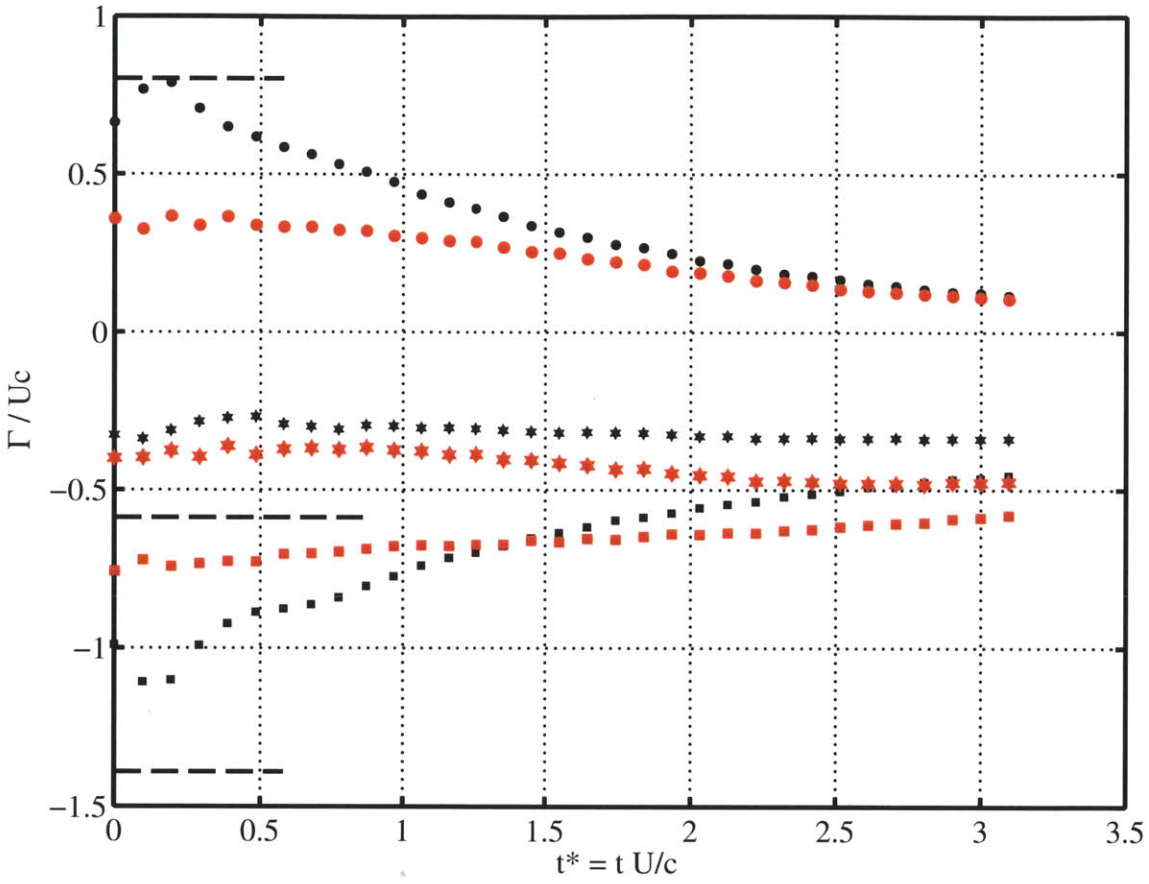

Figure 4-3: Subset of data of Figure 4-2, for clarity. Averaged total positive circulation, total negative circulation, and net circulation calculated at each time step. Please refer to Figure 2-7: black lines correspond to experiment *(a)*, and red lines to experiment *(d)*. Circulation derived from potential flow for a Joukowski foil with similar foil geometry also plotted for theoretical reference. Total positive circulation, total negative circulation, as well as total net circulation are plotted according to the symbols: ■ – Negative Circulation, ● – Positive Circulation ✸ – Net Circulation, Dashed Line - Joukowski Foil.

Chapter 5

Discussion

5.1 Number and pattern of vortices

Our main goal, as introduced previously in this work, is to determine the pattern of vortices formed after the global vorticity shedding event occurs. We have shown in the previous results sections what happens to the shed vorticity once the vanishing event occurs. We refer to a summary of the results in Figure 5-1. The top row of the figure shows three time steps of the ensembled vorticity field for the half streamlined foil experiment, and the bottom row shows the corresponding time steps seen in the square-tipped foil experiment. In the square-tipped foil case, two primary vortices are formed very soon after the vanishing event, and not long after that the secondary vortices can be seen to appear in the PIV plane, as shown in the bottom panel at $t^* = 0.05$. The secondary vortices then grow and begin the amalgamate back into the primary vortices as time goes on, as shown in the bottom panel at $t^* = 0.20$, and eventually the primary and secondary vortices have amalgamated into the two lasting vortices left in the wake, as seen in the bottom panel at $t^* = 1.00$. For the half streamlined case, we look to the top panel of the figure. We can see here that once the shear layers have been deposited in the fluid, right after the vanishing event (defined as when the entire cross section of the foil disappears from the plane), there is no appearance of secondary vortices and the shear layers seem to calmly and continuously roll up into the two lasting vortices in the wake. A feature to note here

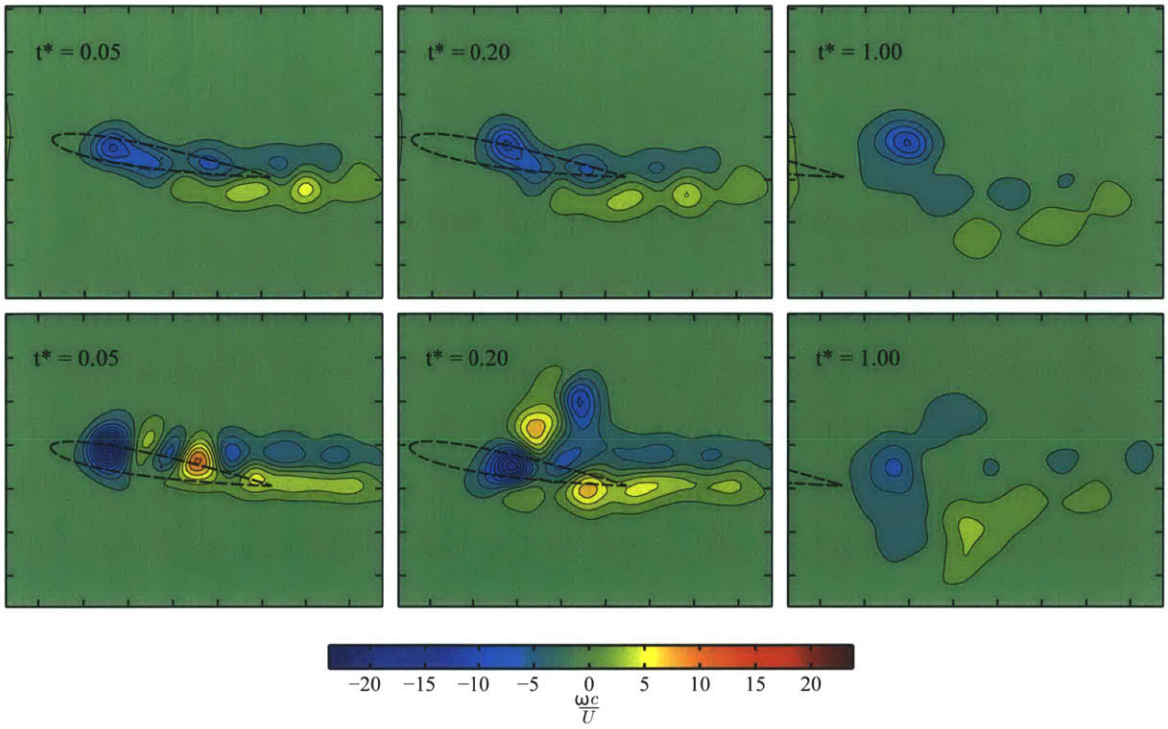

Figure 5-1: Summary of the PIV results for the square and half-chord streamlined foils experiments. Top row shows three time steps of the ensemble-averaged vorticity field for the square case, and bottom row shows corresponding time steps for the half-chord streamlined foil case.

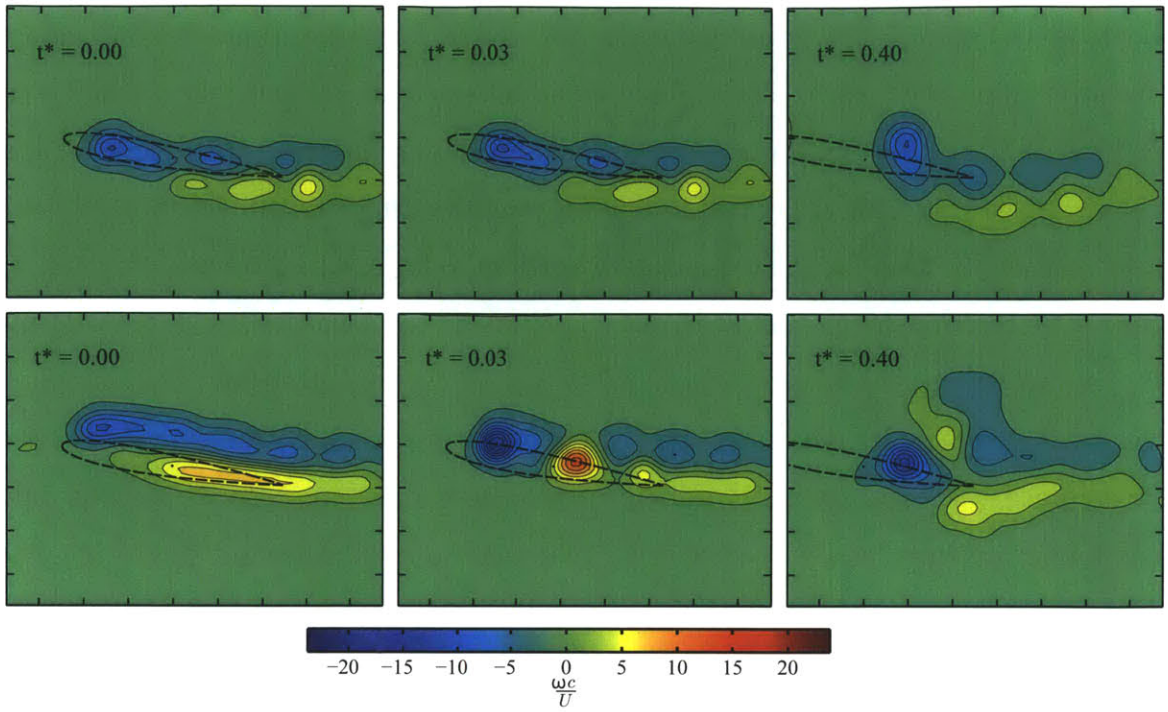

Figure 5-2: Comparison of vortex formation times for the square foil case and the half-chord streamlined foil case.

is that in the square case, we have two lasting vortices dominating the wake with smaller patches of vorticity, but in the streamlined-end case the wake looks more like one dominating lasting vortex with a few smaller patches of vorticity. This could be useful in terms of practical use, because a wake dominated by one lasting vortex is simpler to predict and control than a wake with two dominant vortices.

Overall, we have seen that pattern of vortex formation for the square foil case involves the evolution of two primary and two secondary vortices that amalgamate into two lasting vortices in the wake, whereas for the streamlined-end foil cases the pattern of vortex formation is much simpler, with the deposited shear layers continuously rolling up to form one dominant lasting vortex in the wake.

5.2 Vortex Formation Times

Another measure of utility is the time it takes for the vortices to form; we want to be able to use the strength of the vorticity when the vortex has fully formed.

Looking at Figure 5-2, we can determine the vortex formation times for our square and streamlined-end cases. The top row shows relevant time steps for the streamlined-end case, and the bottom row shows the corresponding time steps for the square case. For the square case, there are two formation times we can pick out. The first of these is the formation time for the two primary vortices to form, which occurs a very short time after the vanishing event at $t^* = 0.03$. Next, we can identify the formation time for the two lasting vortices to be around $t^* = 0.40$. Around this time the features of the lasting vortices become clear and the two vortices are essentially formed. For the streamlined-end case, since the rolling up process is more continuous, there is only one formation time, and we can identify that time to also be around $t^* = 0.40$. The formation times for our vanishing foils are quite small.

By comparison, the vortex ring formation time presented in Gharib *et al* (1998) [10] is an order of magnitude larger than the longest formation time presented in this work. In Gharib *et al*, a piston-cylinder system slowly feeds vorticity into the free fluid, with the resulting vortex ring fully formed at the specified non-dimensional formation time of $t^* = tU/c \approx 4$. In our vanishing foil, we have nearly instantaneous vortex formation at $t^* = tU/c \approx 0.4$ because vorticity here is *globally* shed *at once*. While the shedding of vorticity into a vortex ring from a piston and cylinder is not exactly analogous to the phenomenon of global vorticity shedding, the comparison underlines the fundamental difference between traditional vortex shedding and global vorticity shedding: global vorticity shedding is so much faster than traditional shedding because the vorticity is shed all around the body and all at once.

5.3 Potential Flow Force Estimates: Streamlined-end and Square-tipped Foils

As a simple estimate of what forces we might be able to extract from this phenomenon, we can imagine a hypothetical setup with a towed foil with a cylinder towed behind it; see Figure 5-3. Both foil and cylinder would be towed at speed U, so that the relative

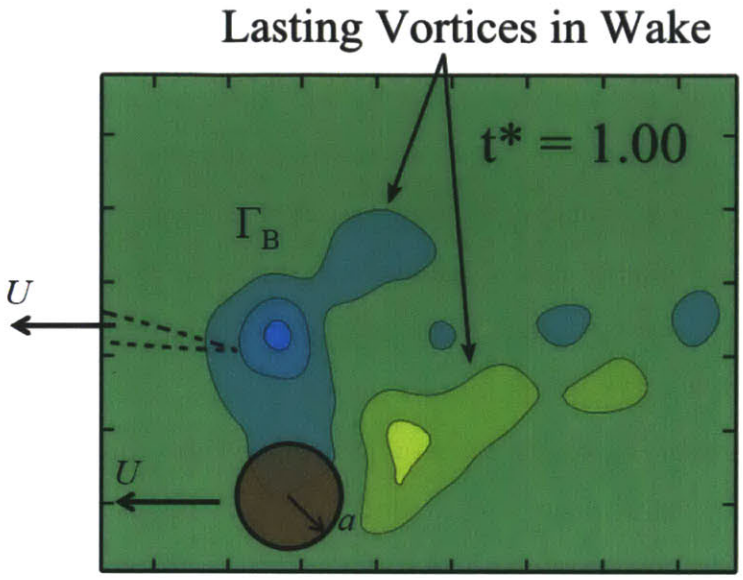

Figure 5-3: Simple hypothetical setup to estimate the vortex force in potential flow on a cylinder placed behind the vanished foil, with both towed at speed U.

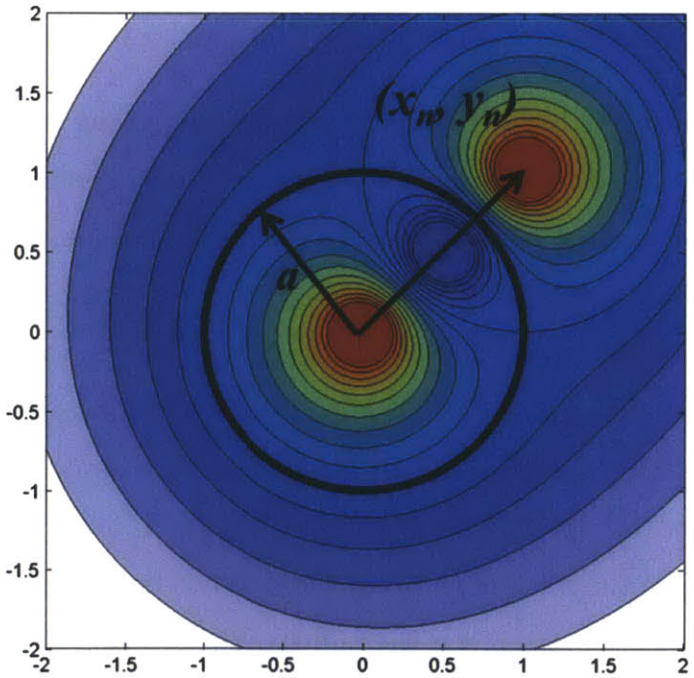

Figure 5-4: Contour plot of the stream function (imaginary part of the complex potential) demonstrating the circle theorem: a vortex and a cylinder of radius a in potential flow is represented by an external vortex located at (x_n, y_n), and two vortices inside the radius a.

distance between them does not change. The foil would vanish as before, and in our hypothetical situation the lasting vortices in the vanished foil wake would interact with the towed cylinder to provide a suction-like force. We can use our experimental data, along with potential flow theory, to provide a rough estimate on the magnitude of force we could extract from our lasting vortices in the wake. This hypothetical setup and the following potential flow simplifications are by no means the ideal method of utilizing the global vorticity phenomenon, and are only introduced to provide a rough estimate of forces a vortex would induce on a cylinder.

In our estimate of the vortex force on the cylinder, for simplification we will take into account only the stronger vortex (labeled Γ_B in Figure 5-3) and will consider the vortex to be a point vortex. The formula for the vortex force on a cylinder in potential flow is shown below: [7], [16]

$$F_y = \rho\Gamma_n a^2 \left(\frac{u_n \left(x_n^2 - y_n^2\right) + 2v_n x_n y_y}{\left(x_n^2 + y_n^2\right)^2} \right) - \frac{\rho\Gamma_n^2}{2\pi} \left(\frac{y_n}{a^2 - \left(x_n^2 + y_n^2\right)} + \frac{y_n}{x_n^2 + y_n^2} \right)$$

This formula is derived from integrating the pressure along the cylinder body surface, using Bernoulli's unsteady equation and the complex potential that represents a cylinder in the flow with a point vortex. The complex potential that is used consists of the real vortex external to the cylinder and two vortices inside the cylinder radius. With these three vortices in the appropriate locations, the radius of the cylinder becomes a streamline, and thus, these three vortices form a potential flow that represents an external point vortex near a cylinder. An illustrative example showing the contour plot of the stream function demonstrates this idea (Figure 5-4 [1]). In the above formula, F_y is the lift force on the cylinder, ρ is the density of the fluid, Γ_n is the circulation of the n^{th} vortex, a is the radius of the cylinder, (x_n, y_n) is the position of the n^{th} vortex relative to the cylinder, and (u_n, v_n) is the velocity of the n^{th} vortex relative to the cylinder. For n vortices, the total lift force is found by summing the above equation over all n.

[1] Figure 5-4 adapted from http://www.bugman123.com/GANNAA/indew.html

For detailed derivation of the vortex force on a cylinder in potential flow, see Appendix B of Dahl (2008). [7] For background reading on the circle theorem and the Blasius theorem for complex potentials, see Milne (1962). [16]

To estimate the vortex force in our hypothetical setup, we need a few numbers. First, we choose to estimate the force for the square case at $t^* = 1.00$. At this time step the wake is fully developed. Referring to our previous calculations, shown in Figure 4-2, the circulation of vortex Γ_B at $t^* = 1.00$ is about $0.75 \cdot Uc$. We choose the radius of our hypothetical cylinder to be the thickness of the foil, so that $a = t = .12 \cdot c$. We can also choose the relative position of the vortex to be above the cylinder at $(x_B, y_B) = (0, 1.5a)$. We also know that since our cylinder and foil are towed at speed U to the left and that the lasting vortices, once deposited, advect very slowly, we can estimate the relative velocity of the vortex to be speed U to the right so that $(u_B, v_B) = (0.2\,\mathrm{m/s}, 0)$. Using these numbers from our data, we estimate the vortex force on the cylinder to be 2.0 N, when normalized by $\frac{1}{2}\rho U^2 c$ results in a "lift" coefficient of 1.4. For some sort of comparison, the experimental lift coefficient on the steady state towed foil at 10 deg is 0.8, and as stall begins to occur at this angle of attack, we cannot get a higher lift coefficient on the steadily translating foil than 0.8. Thus, we are able to produce a respectable lift force on the hypothetical cylinder.

Chapter 6

Conclusions

In this thesis we have explored several different aspects of the phenomenon we call global vorticity shedding. Global vorticity shedding occurs when an object in viscous fluid suddenly vanishes, shedding the entire boundary layer vorticity into the wake at once. In our experiments we approximate the disappearance of a towed foil by rapidly retracting the foil in the span-wise direction. Global vorticity shedding is in distinct contrast with conventional shedding, in which vorticity is shed from a body from only a few separation points into the fluid. While some theoretical studies have been done on what happens to the vorticity shed from a vanished body, the resulting vortex formation patterns were based on unproven assumptions and hypotheses only. In this work, we have shown what the vortex patterns are for a vanishing foil at an angle of attack.

We have learned from PIV measurements and three-dimensional simulations that for a square-tipped foil, primary and secondary vortices evolve and eventually amalgamate to leave two lasting vortices in the wake. The secondary vortices are a result of three-dimensionality in the flow. For a streamlined-end foil, we achieve a simpler and less three-dimensional wake with no secondary vortices, and only one lasting vortex dominating the wake. However, due to the inherent nature of the streamlined-end foil the initial circulation is reduced. Having a simpler wake is better for vortex control, for future implementations.

We have also seen that our lasting vortices are capable of producing reasonable

forces on a body through simple potential flow estimations. Vortex formation times are also small, with vortices fully formed nearly instantaneously in the flow. These features are promising for a force transducer using global vorticity shedding to impart large and fast maneuvering forces on an underwater vehicle.

For future work, we envision using global vorticity shedding to introduce large and fast maneuvering forces for an underwater vehicle. This future work involves finding an ideal foil geometry, taking force measurements, understanding the interactions of the phenomenon with multiple foils, and setting up a control strategy for vortex control. We have made significant contributions to the understanding of various aspects of global vorticity shedding, and we hope to continue making contributions to the field of ocean engineering and science, in general.

This research was made with Government support under and awarded by DoD, Air Force Office of Scientific Research, National Defense Science and Engineering Graduate (NDSEG) Fellowship, 32 CFR 168a and by the Singapore-MIT Alliance for Research and Technology (SMART).

Bibliography

[1] H. Aref. Integrable, chaotic and turbulent vortex motion in two-dimensional flows. *Annu. Rev. Fluid Mech.*, 15:345–389, 1983.

[2] D. Birch and T. Lee. Investigation of the near-field tip vortex behind an oscillating wing. *J. Fluid Mech.*, 544:201–241, 2005.

[3] P. Blondeaux, F. Fornarelli, L. Guglielmini, M. S. Triantafyllou, and R. Verzicco. Numerical experiments on flapping foils mimicking fish-like locomotion. *Phys. Fluids*, 17:113601, 2005.

[4] J. H. J. Buchholz and A. J. Smits. On the evolution of the wake structure produced by a low-aspect-ratio pitching panel. *J. Fluid Mech.*, 546:433–443, 2006.

[5] J. H. J. Buchholz and A. J. Smits. The wake structure and thrust performance of a rigid low-aspect-ratio pitching panel. *J. Fluid Mech.*, 603:331–365, 2008.

[6] S. Childress, N. Vandenberghe, and J. Zhang. Hovering of a passive body in an oscillating airflow. *Phys. Fluids*, 18:117103, 2006.

[7] Jason Dahl. *Vortex-Induced Vibration of a Circular Cylinder with Combined In-line andCross-flow Motion.* PhD thesis, MIT, Mechanical and Ocean Engineering Department, 2008.

[8] H. Dong, M. Bozkurttas, R. Mittal, P. Madden, and G. V. Lauder. Computational modelling and analysis of the hydrodynamics of a highly deformable fish pectoral fin. *J. Fluid Mech.*, 645:345–373, 2010.

[9] Pschl Th. Ewald, P.P and L. Prandtl. *The physics of solids and fluids,with recent developments.* Blackie & Son Limited, 1936.

[10] M. Gharib, E. Rambod, and K. Shariff. A universal time scale for vortex ring formation. *J. Fluid Mech.*, 360:121–140, 1998.

[11] T. Y. Hubel, N. I. Hristov, S. M. Schwartz, and K. S. Breuer. Time-resolved wake structure and kinematics of bat flight. *Exp. in Fluids*, 46:933–943, 2009.

[12] J. Jeong and F. Hussain. On the identification of a vortex. *J. Fluid Mech.*, 285:69–94, 1995.

[13] L. C. Johansson and R. A. Norberg. Delta-wing function of webbed feet gives hydrodynamic lift for swimming propulsion in birds. *Nature*, 424:65–68, 2003.

[14] F. Klein. Über die bildung von wirbeln in reibungslosen flüssigkeiten. *Z. Mathematik & Physik*, 58:259–262, 1910.

[15] L. G. Margolin, W. J. Rider, and F. F. Grinstein. Modeling turbulent flow with implicit LES. *J. Turbul.*, 7, 2007.

[16] L. M. Milne-Thomson. *Theoretical Hydrodynamics*. St Martin's Press Inc, 1962.

[17] B. R. Morton. The generation and decay of vorticity. *Geophys. Astrophys. Fluid Dynamics*, 28:277–308, 1984.

[18] U. K. Müller and D. Lentink. Physiology - turning on a dime. *Science*, 306:1899–1900, 2004.

[19] L. Prandtl. Die entstehung von wirbeln in einer flüssigkeit kleinster reibung. *Zeitschrift für Flugtechnik und Motorluftschiffahrt*, 18:489–496, 1927.

[20] S. E. Spagnolie and M. J. Shelley. Shape-changing bodies in fluid: Hovering, ratcheting, and bursting. *Phys. Fluids*, 21:013103, 2009.

[21] Jordan Stanway. The turtle and the robot: An old sea turtle teaches a young engineer a thing or two about swimming. Oceanus Magazine, 2008. www.whoi.edu/oceanus.

[22] S. Taneda. Visual study of unsteady separated flows around bodies. *Prog. Aerosp. Sci.*, 17:287–348, 1977.

[23] G. I. Taylor. Formation of a vortex ring by giving an impulse to a circular disk and then dissolving it away. *J. Appl. Phys.*, 24:104, 1953.

[24] K. D. von Ellenrieder, K. Parker, and J. Soria. Flow structures behind a heaving and pitching finite-span wing. *J. Fluid Mech.*, 490:129–138, 2003.

[25] G. D. Weymouth, D. G. Dommermuth, K. Hendrickson, and D. K.-P. Yue. Advancements in cartesian-grid methods for computational ship hydrodynamics. In *26th Symposium on Naval Hydrodynamics*, 2006.

[26] G. D. Weymouth and D. K.-P. Yue. Boundary data immersion method for cartesian-grid simulations of fluid-body interaction problems. *J. Comput. Phys.*, In review.

[27] Martin S. Wibawa. Vorticity transfer through rapid area change. Master's project, MIT, Mechanical and Ocean Engineering Department, 2010.